

Single-Stage Wireless-Power-Transfer Resonant Converter With Boost Bridgeless Power-Factor-Correction Rectifier

Junwei Liu¹, Ka Wing Chan, *Member, IEEE*, Chi Yung Chung, *Fellow, IEEE*, Nelson Hon Lung Chan, Ming Liu, and Wenzheng Xu

Abstract—Wireless power transfer (WPT) has drawn more and more attention and has many applications, such as wireless electric vehicle charging systems, which require high power, high efficiency, and high power factor. In this paper, a single-stage WPT resonant converter with bridgeless boost power-factor-correction (PFC) rectifier is proposed to improve efficiency and power quality of line input, and reduce production cost and complexity for high-power WPT system. The bridgeless single-stage topology is creatively proposed to apply in WPT system, which is much more advantageous than conventional two-stage WPT converter with individual boost PFC stage.

Index Terms—Bridgeless, power factor correction (PFC), single stage, wireless power transfer (WPT).

I. INTRODUCTION

WIRELESS power transfer (WPT) is taking up more and more roles in industrial community. WPT technology has a variety of applications with power levels ranged from several milliwatts to tens of kilowatts, including charging portable telephone [1], supplying power for biomedical implants [2]–[4], electric vehicle (EV) battery charging [5], [6], and road-way powering moving EVs [7], [8]. Compared to conventional wired power transmission, WPT technology is much more advantageous: convenient, safe, and reliable. Inductive coupling method [1], [2], [6]–[14], as a traditional WPT technology, has been researched for a long time and is a very efficient way to deliver power wirelessly within a short distance. However, power and efficiency drop severely if transfer distance extends or there is a misalignment between transmitter and receiver. Another efficient WPT technology for midrange transfer, magnetic resonant coupling approach [15]–[20], proposed and demonstrated

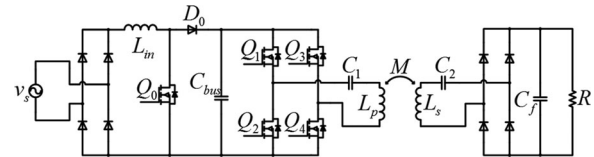


Fig. 1. Conventional AC/DC WPT resonant converter with boost PFC.

by MIT in 2007 [21], attracts much interest from researchers in recent years, due to its high efficiency and relatively longer transfer distance. This approach utilizes resonance characteristic of coupled primary and secondary resonant tanks under a specific frequency to achieve WPT efficiently. A conventional WPT system consists of a single-phase electric power supply, a full-bridge rectifier, a boost power factor corrector (PFC), a dc bus capacitor, a high-frequency inverter, coupled primary and secondary resonant tanks, a secondary high-frequency rectifier bridge, a filter capacitor, and a load resistor, as shown in Fig. 1.

Traditional ac/dc converter with PFC usually employs a two-stage topology. The first stage is a boost PFC converter and the second is a dc/dc conversion stage.

Like the WPT system in Fig. 1, the first stage includes a full-bridge rectifier and a boost PFC, and the second stage is a dc/dc WPT resonant converter. It is obvious that such two-stage topology cannot achieve the highest efficiency due to more power losses in the two-stage conversion while it is also not the most economical as more components would be required for two-stage conversion. In recent years, single-stage topologies [22], [23] that integrate both PFC and dc/dc conversion into one power conversion stage have been proposed to overcome the aforementioned drawbacks. Most existing research works are mainly focused on applying single-stage topologies in full-bridge converter [24], half-bridge converter [25], LLC converter [26]–[28], forward converter [29], flyback converter [30], [31], and so on, with most of them designed for small power applications. In this paper, a novel single-stage topology is proposed and applied to high-power WPT systems with improved efficiency and lower cost. Furthermore, based on this single-stage technique, bridgeless boost PFC rectifiers [32]–[35] are introduced and integrated in the WPT system. Bridgeless boost PFC rectifiers would have less conduction loss due to less number of semiconductor devices being involved. Therefore, the newly

Manuscript received March 31, 2017; revised July 6, 2017; accepted July 20, 2017. Date of publication August 25, 2017; date of current version December 15, 2017. This work was supported by the Department of Electrical Engineering, The Hong Kong Polytechnic University. (Corresponding author: Junwei Liu.)

J. Liu, K. W. Chan, N. H. L. Chan, M. Liu, and W. Xu are with the Department of Electrical Engineering, The Hong Kong Polytechnic University, Hong Kong (e-mail: liujunwei_hust@hotmail.com; eekwchan@polyu.edu.hk; nelson06@gmail.com; leo.m.liu@connect.polyu.hk).

C. Y. Chung is with the Department of Electrical and Computer Engineering, University of Saskatchewan, Saskatoon, SK S7N 5A9, Canada (e-mail: c.y.chung@usask.ca).

Color versions of one or more of the figures in this paper are available online at <http://ieeexplore.ieee.org>.

Digital Object Identifier 10.1109/TIE.2017.2745471

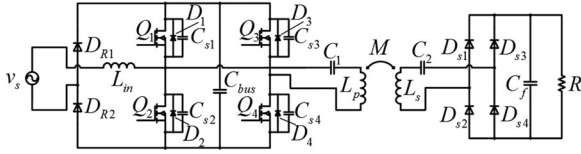


Fig. 2. Proposed novel topology—single-stage WPT resonant converter with front-end bridgeless boost PFC rectifier.

proposed converter can reduce losses and cost further while the high performance of the PFC function can be maintained. Compared to the single-stage Z-source resonant converter proposed in [36] for WPT application, the newly proposed converter is advantageous in terms of efficiency and number of semiconductor devices and passive components.

In this paper, the topology description and analysis, power factor (PF) and total harmonics distortion (THD) analysis, modulation method, and circuit operation of the proposed converter with a new control approach are first presented, and then, the design procedure with an example is proposed. In addition, a new and more accurate analytical and calculation method considering both the fundamental and higher order components is also proposed to analyze the dc/dc WPT converter. Finally, an experimental prototype is implemented to verify the analysis and design.

II. PROPOSED SINGLE-STAGE TOPOLOGY

A. Circuit Description

Fig. 2 shows the proposed novel topology—single-stage WPT resonant converter with bridgeless boost PFC rectifier, which ultimately integrates the front-end full-bridge rectifier, boost PFC, and full-bridge inverter in the primary side together. v_s is ac input voltage, D_{R1} and D_{R2} are front-end bridgeless rectifier diodes, L_{in} is input inductor, C_{bus} is bus capacitor, $Q_1 - Q_4$ are four MOSFET switches (with body diodes $D_1 - D_4$), $C_{s1} - C_{s4}$ are snubber capacitors of the switches, C_1 and C_2 are capacitors of primary and secondary resonant tanks, L_p and L_s are inductors of primary and secondary resonant tanks, M is mutual inductance of L_p and L_s , $D_{s1} - D_{s4}$ are secondary-side rectifier diodes, C_f is output filtering capacitor, and R is load resistor. Compared with the conventional topology in Fig. 1, a half-bridge of the full-bridge rectifier, the switch Q_0 , and the diode D_0 (totally four semiconductor devices) are eliminated. In the proposed topology, Q_1 and Q_2 perform two functions: 1) realization of PFC: they act as D_0 and Q_0 as shown in Fig. 1 for PFC, and 2) combination with Q_3 and Q_4 to form the full-bridge inverter of the dc/dc WPT resonant converter.

B. Bridgeless Boost PFC Rectifier

Fig. 3(a) shows the bridgeless boost PFC rectifier of the proposed topology, which consists of rectifier diodes D_{R1} and D_{R2} , input inductor L_{in} , half-bridge switches Q_1 and Q_2 , and bus capacitor C_{bus} . Fig. 3(b) shows the operations in positive and negative line cycle. In fact, whenever in positive or negative line cycle, the bridgeless boost PFC rectifier can act as a boost

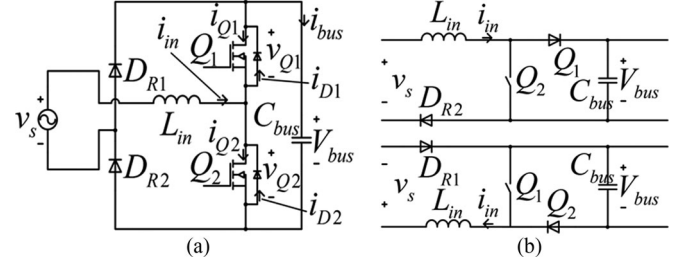


Fig. 3. Bridgeless boost PFC rectifier.

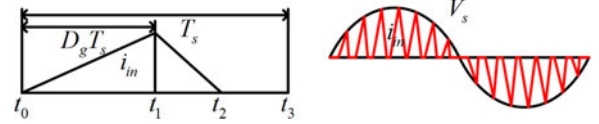


Fig. 4. Waveforms of input current.

converter to fulfill PFC function. Here, upper equivalent circuit in Fig. 3(b) is taken as an example to analyze its characteristics.

1) Working Principle and Analysis: As shown in Fig. 4, the input inductor must work in discontinuous conduction mode (DCM) in order to reduce the higher order harmonics in the line current [25], [26], [30], [37]. When switch Q_2 is ON, voltage across L_{in} is v_s , and the input current i_{in} flowing through L_{in} is given by

$$di_{in}/dt = v_s/L_{in}. \quad (1)$$

When Q_2 is OFF, v_{Q2} is equal to V_{bus} (bus voltage) and the voltage across L_{in} is $v_s - V_{bus}$, then i_{in} is given by

$$di_{in}/dt = (v_s - V_{bus})/L_{in}. \quad (2)$$

For a complete cycle of switching period T_s , i_{in} is expressed as

$$i_{in} = \begin{cases} (v_s/L_{in}) \cdot t & t \in [t_0, t_1] \\ (V_{bus}/L_{in}) \cdot (t_1 - t_0) - ((V_{bus} - v_s)/L_{in}) \cdot t & t \in [t_1, t_2] \\ 0 & t \in [t_2, t_3] \end{cases} \quad (3)$$

where $t_0 - t_3$ are defined as (D_g is duty ratio of the switch)

$$t_0 = 0, t_1 = D_g T_s, t_2 = D_g T_s (V_{bus}/(V_{bus} - v_s)), t_3 = T_s. \quad (4)$$

To make input inductor work in DCM, t_2 must be smaller than or equal to t_3 , which means (peak value of v_s noted as V_{sp})

$$D_g T_s (V_{bus}/(V_{bus} - v_s)) \leq T_s \Rightarrow V_{sp}/V_{bus} \leq 1 - D_g. \quad (5)$$

Therefore, the average input power in a switching period T_s is

$$P_T(t) = \left(\int_{t_0}^{t_3} v_s(t) i_{in}(t) dt \right) / T_s = \frac{D_g^2 v_s(t)^2 T_s V_{bus}}{2 L_{in} (V_{bus} - v_s(t))}. \quad (6)$$

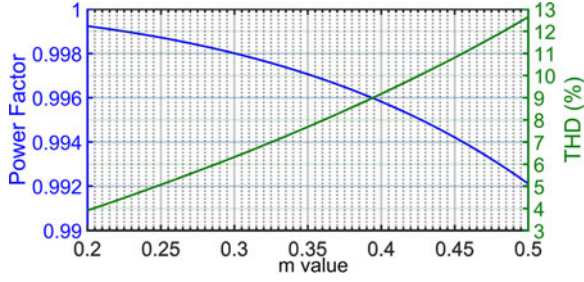


Fig. 5. Relations of m value versus PF and THD_i .

For a line cycle, the average input power is

$$P_{\text{in}} = \left[\int_0^{T_l} P_T(t) dt \right] / T_l = \frac{D_g^2 V_{sp}^2}{2\pi L_{\text{in}} f_s} \int_0^\pi \frac{(\sin \alpha)^2}{1 - m \sin \alpha} d\alpha \quad (7)$$

where T_l is line period, and m is V_{sp}/V_{bus} .

2) Analysis of PF and THD_i : The average value of i_{in} during a switching period is given as

$$i_{\text{in,avg}} = \frac{1}{T_s} \int_0^{T_s} i_{\text{in}} dt = D_g^2 \cdot \frac{V_{sp}}{2L_{\text{in}} f_s} \cdot \frac{\sin(\omega_l t)}{1 - m |\sin(\omega_l t)|} \quad (8)$$

where ω_l is the line frequency in radian. Because of the symmetric characteristics for both positive and negative half-cycles of v_s , the root-mean-square (rms) values of input current i_{in} for positive and negative half-cycles of v_s are equal. Therefore, the rms value of input current i_{in} for T_l is as follows:

$$i_{\text{in,rms}} = \frac{D_g^2 V_{sp}}{2\sqrt{\pi} L_{\text{in}} f_s} \sqrt{\int_0^\pi \frac{(\sin \alpha)^2}{(1 - m |\sin \alpha|)^2} d\alpha}. \quad (9)$$

Therefore, the PF of the proposed converter is obtained

PF =

$$\left(\sqrt{2} \int_0^\pi \frac{(\sin \alpha)^2}{1 - m \sin \alpha} d\alpha \right) / \left(\sqrt{\pi} \sqrt{\int_0^\pi \frac{(\sin \alpha)^2}{(1 - m \sin \alpha)^2} d\alpha} \right). \quad (10)$$

From (10), the PF of the proposed converter is only related to m (equal to V_{sp}/V_{bus}), as shown in Fig. 5 (curve in blue).

For THD_i (THD of input current i_{in}) analysis, $i_{\text{in,avg}}$ can be expressed as Fourier series

$$i_{\text{in,avg}}(t) = b_1 \sin(\omega_l t) + b_3 \sin(3\omega_l t) + b_5 \sin(5\omega_l t) + \dots$$

$$b_n = (2/T_l) \int_0^{T_l} i_{\text{in,avg}}(t) \sin(n\omega_l t) dt \quad n = 1, 3, 5, \dots \quad (11)$$

and THD_i can be obtained

$$\text{THD}_i = \sqrt{b_3^2 + b_5^2 + b_7^2 + \dots} / b_1. \quad (12)$$

By analysis and calculation, THD_i is also only related to m value, as shown in Fig. 5 (curve in green).

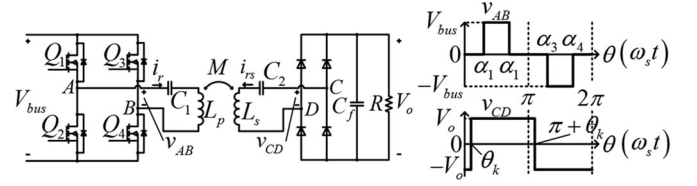


Fig. 6. DC/DC WPT resonant converter and waveforms of v_{AB} and v_{CD} for theoretical analysis.

C. DC/DC WPT Resonant Converter

After the front-end bridgeless boost PFC rectifier stage is the dc/dc WPT resonant converter applying resonant magnetic coupling technology to realize midrange WPT. Such converter, also called dc/dc resonant converter for WPT, is shown as left part of Fig. 6, where V_{bus} is the bus voltage, or dc input voltage of the converter, V_o is output voltage, v_{AB} and v_{CD} are voltages across primary and secondary sides of resonant tank. By adjusting switching sequence and duty ratios of switches $Q_1 - Q_4$, v_{AB} can be regulated to be a three-level voltage with adjustable duty ratio D_{ab} , shown as the right part of Fig. 6.

First harmonic approximation (FHA) [38], which only considers fundamental component, is commonly applied to analyze dc characteristics of resonant converters. If FHA is applied here, (13)–(15) will be obtained

$$v_{AB} = [1/(j\omega_s C_1) + j\omega_s L_p] \cdot i_r + j\omega_s M \cdot i_{rs} \quad (13)$$

$$0 = j\omega_s M \cdot i_r + [1/(j\omega_s C_2) + j\omega_s L_s] \cdot i_{rs} + R_e \cdot i_{rs} \quad (14)$$

$$v_{CD} = -i_{rs} \cdot R_e \quad (15)$$

where R_e is equivalent resistor

$$R_e = (8/\pi^2) \cdot R. \quad (16)$$

From (13) to (15), voltage transfer gain of the resonant tank can be obtained

$$\left| \frac{v_{CD}}{v_{AB}} \right| = 1 / \sqrt{\left(\frac{L_p/M - 1/(\omega_s^2 C_1 M)}{\omega_s^4 L_p L_s C_1 C_2 - \omega_s^2 (C_2 L_s + C_1 L_p) + 1} - \frac{\omega_s M}{R_e} \right)^2}. \quad (17)$$

And dc voltage transfer gain is

$$V_o/V_{\text{bus}} = \sin(D_{ab}\pi/2) \cdot |v_{CD}/v_{AB}|. \quad (18)$$

By analysis, there are three resonant frequencies [11]

$$\omega_1 = [(L_p + M \cdot k) C_1]^{-1/2} = [(L_s + M/k) C_2]^{-1/2}$$

$$\omega_2 = [(L_p - M \cdot k) C_1]^{-1/2} = [(L_s - M/k) C_2]^{-1/2}$$

$$\omega_3 = (L_p C_1)^{-1/2} = (L_s C_2)^{-1/2} \quad (19)$$

where k is defined as square root of L_p/L_s . Voltage transfer gain of the resonant tank is independent of load resistance at ω_1 and ω_2 , whereas at ω_3 , it is directly proportional to load resistance [39].

However, such approximation is not accurate enough for analyzing the converter when duty ratio and load power are small because there are nonnegligible higher order harmonics exiting

in the circuit. For accurate analysis, both fundamental component and higher order harmonics shall be considered.

Current flowing through L_s is always continuous at most load conditions except in very low load conditions. Therefore, in this paper only the conditions of L_s in continuous current mode are analyzed. By analyzing the behavior of the converter, v_{AB} is a three-level voltage with duty ratio D_{ab} and v_{CD} is a two-level voltage with 50% duty ratio, as shown in Fig. 6, where θ is equal to $\omega_s t$, ω_s is operating frequency in radian, θ_k is the phase angle of v_{CD} , and $\alpha_1 - \alpha_4$ are defined as

$$\alpha_{1,2} = (1 \mp D_{ab})\pi/2, \quad \alpha_{3,4} = (3 \mp D_{ab})\pi/2. \quad (20)$$

Hence, v_{AB} and v_{CD} can be expressed as Fourier series

$$v_{AB} = v_{AB,1} + v_{AB,3} + v_{AB,5} + \dots + v_{AB,n} + \dots \quad (21)$$

$$v_{CD} = v_{CD,1} + v_{CD,3} + v_{CD,5} + \dots + v_{CD,n} + \dots \quad (22)$$

where

$$v_{AB,n} = V_{AB,ns} \sin(n\omega_s t) + V_{AB,nc} \cos(n\omega_s t) \quad (23)$$

$$v_{CD,n} = V_{CD,ns} \sin(n\omega_s t) + V_{CD,nc} \cos(n\omega_s t) \quad (24)$$

and $V_{AB,ns}$, $V_{AB,nc}$, $V_{CD,ns}$, and $V_{CD,nc}$ ($n = 1, 3, 5, \dots$) are calculated

$$\begin{aligned} V_{AB,ns} = \\ (-1)^{(n-1)/2} \cdot 4V_{bus} \sin(nD_{ab}\pi/2)/(n\pi), V_{AB,nc} = 0 \end{aligned} \quad (25)$$

$$\begin{aligned} V_{CD,ns} = \\ 4V_o \cos(n\theta_k)/(n\pi), V_{CD,nc} = -4V_o \sin(n\theta_k)/(n\pi). \end{aligned} \quad (26)$$

i_r and i_{rs} are currents through L_p and L_s , v_{c1} and v_{c2} are voltages across C_1 and C_2 , also shown in Fourier series

$$i_r = i_{r,1} + i_{r,3} + i_{r,5} + \dots + i_{r,n} + \dots \quad (27)$$

$$i_{rs} = i_{rs,1} + i_{rs,3} + i_{rs,5} + \dots + i_{rs,n} + \dots \quad (28)$$

$$v_{c1} = v_{c1,1} + v_{c1,3} + v_{c1,5} + \dots + v_{c1,n} + \dots \quad (29)$$

$$v_{c2} = v_{c2,1} + v_{c2,3} + v_{c2,5} + \dots + v_{c2,n} + \dots \quad (30)$$

where

$$i_{r,n} = I_{r,ns} \sin(n\omega_s t) + I_{r,nc} \cos(n\omega_s t) \quad (31)$$

$$i_{rs,n} = I_{rs,ns} \sin(n\omega_s t) + I_{rs,nc} \cos(n\omega_s t) \quad (32)$$

$$v_{c1,n} = V_{c1,ns} \sin(n\omega_s t) + V_{c1,nc} \cos(n\omega_s t) \quad (33)$$

$$v_{c2,n} = V_{c2,ns} \sin(n\omega_s t) + V_{c2,nc} \cos(n\omega_s t). \quad (34)$$

Applying Kirchhoff's voltage law, (35)–(38) are obtained

$$v_{AB} = L_p (di_r/dt) + v_{c1} + M (di_{rs}/dt) \quad (35)$$

$$i_r = C_1 (dv_{c1}/dt) \quad (36)$$

$$v_{CD} = L_s (di_{rs}/dt) + v_{c2} + M (di_r/dt) \quad (37)$$

$$i_{rs} = C_2 (dv_{c2}/dt). \quad (38)$$

From (21) to (24), and (27) to (38), we have

$$V_{AB,ns} = -Z_{pn} I_{r,nc} - Z_{mn} I_{rs,nc} \quad (39)$$

$$V_{AB,nc} = Z_{pn} I_{r,ns} + Z_{mn} I_{rs,ns} \quad (40)$$

$$V_{CD,ns} = -Z_{sn} I_{rs,nc} - Z_{mn} I_{r,nc} \quad (41)$$

$$V_{CD,nc} = Z_{sn} I_{rs,ns} + Z_{mn} I_{r,ns} \quad (42)$$

where Z_{pn} , Z_{mn} , and Z_{sn} ($n = 1, 3, 5, \dots$) are defined as

$$\begin{aligned} Z_{pn} = n\omega_s L_p \\ - \frac{1}{n\omega_s C_1}, \quad Z_{mn} = n\omega_s M, \quad Z_{sn} = n\omega_s L_s - \frac{1}{n\omega_s C_2}. \end{aligned} \quad (43)$$

Output power can be expressed as

$$P_o = (1/\pi) \int_{\theta_k}^{\pi+\theta_k} V_o (-i_{rs}) d\theta = V_o^2 / R. \quad (44)$$

From characteristic of the secondary-side rectifier bridge, at $\omega_s t = \theta_k$, i_{rs} is equal to zero, therefore

$$i_{rs}(\theta_k) = i_{rs,1}(\theta_k) + i_{rs,3}(\theta_k) + \dots + i_{rs,n}(\theta_k) + \dots = 0. \quad (45)$$

And (46) and (47) can be derived from (20) to (45)

$$\begin{aligned} \frac{8V_o V_{bus}}{\pi^2} \sum_{n=1,3,5,\dots} \frac{(-1)^{\frac{n-1}{2}} Z_{mn} \sin(nD_{ab}\pi/2) \sin(n\theta_k)}{n^2 (Z_{pn} Z_{sn} - Z_{mn}^2)} \\ = \frac{V_o^2}{R} \\ \sum_{n=1,3,5,\dots} \frac{(-1)^{\frac{n-1}{2}} Z_{mn} V_{bus} \sin(nD_{ab}\pi/2) \cos(n\theta_k) - Z_{pn} V_o}{n (Z_{pn} Z_{sn} - Z_{mn}^2)} \\ = 0. \end{aligned} \quad (46)$$

In this paper, balancing calculation complexity and accuracy, fundamental (first-order), third-order, and fifth-order components are considered in the calculation to analyze the dc characteristics of the proposed WPT resonant converter. By solving (46) and (47), V_o/V_{bus} and θ_k are calculated.

D. Modulation Method and Circuit Operation

1) Description of Proposed Modulation Method: Usually frequency control methods are applied in variable kinds of resonant converters. However, frequency control method is not suitable for the proposed topology. From (7), (46), and (47), if D_{ab} is set constantly 1, by increasing operation frequency f_s , P_{in} and P_o will be regulated to low level. However, such regulation will lead to very large V_{bus} , usually larger than 1 kV, which requires bus capacitor and all primary-side semiconductor devices with high-voltage rating and causes severe electromagnetic interference (EMI) problem because of high dv/dt .

Here, a new control approach is proposed to allow the proposed converter to work in a wide-range load condition with high performances (high efficiency, low THD, and high PF). In the proposed control method, D_{ab} is the control parameter to regulate output power with constant V_o when load varies, with

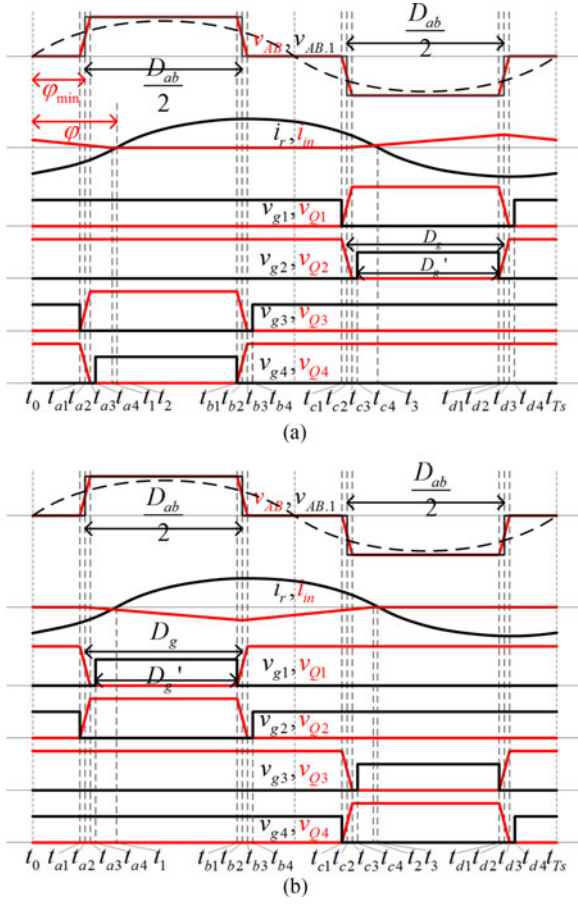


Fig. 7. Operation waveforms of the proposed modulation method: (a) when v_s is in its positive cycle; and (b) when v_s is in its negative cycle.

f_s kept constant within the optimal range of the resonant tank. Make $D_g = D_{ab}/2$, then P_{in} is amended as

$$P_{in} =$$

$$(D_{ab}/2)^2 (V_{sp}^2 / (L_{in}\omega_s)) \int_0^\pi [(\sin \theta)^2 / (1 - m \sin \theta)] d\theta. \quad (48)$$

From (46) to (48), P_{in} and P_o can be easily regulated to low level by adjusting D_{ab} and will not cause very high bus voltage. Therefore, such control method is applied to give a wide-range load regulation.

2) Modulation and Operation Analysis: The proposed modulation and operation waveforms are shown in Fig. 7. Duty ratios of v_{g1} and v_{g2} are noted as D_{g1} and D_{g2} , respectively. Duty ratios of v_{g1} and v_{g2} are complimentary, so are those of v_{g3} and v_{g4} . When v_s is in its positive cycle, D_{g2} is equal to D_g' and v_{g4} leads v_{g2} half a switching period; when v_s is in its negative cycle, D_{g1} is equal to D_g' and v_{g3} lags v_{g1} half a switching period. In an ideal condition, D_g' is equal to D_g . However, in practical implementation considering dead time, D_g' is smaller than D_g . Such modulation method generates a three-level voltage with an adjustable duty ratio. For operation analysis, the proposed topology is simplified to an equivalent circuit shown in Fig. 8.

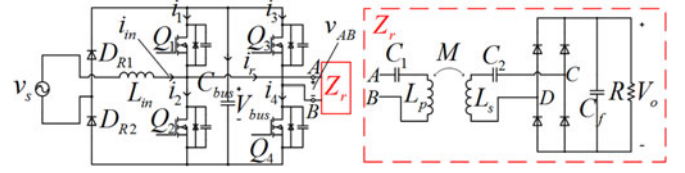


Fig. 8. Equivalent circuit of the proposed topology with resonant tank and secondary side equivalent to impedance Z_r .

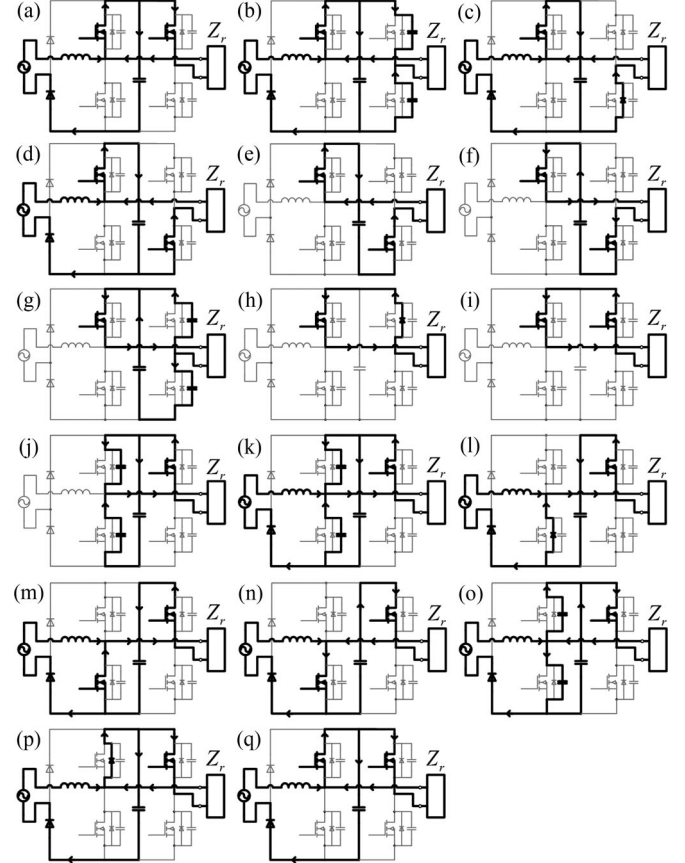


Fig. 9. Operation modes during a switching period for positive half-cycle of input line voltage v_s .

Stage 1 ($t_0 - t_{a1}$): From t_0 to t_{a1} , Q_1 and Q_3 are ON, whereas Q_2 and Q_4 are OFF. Current flows through v_s , L_{in} , Q_1 , C_{bus} , D_{R2} , Q_3 , and Z_r , as shown in Fig. 9(a).

Stage 2 ($t_{a1} - t_{a4}$): At t_{a1} , Q_3 is turned OFF; C_{s3} starts to be charged and C_{s4} starts to be discharged. From t_{a1} to t_{a3} , current flows through v_s , L_{in} , Q_1 , C_{bus} , D_{R2} , C_{s3} , C_{s4} , and Z_r , as shown in Fig. 9(b). At t_{a3} , C_{s3} is charged to V_{bus} and C_{s4} is discharged to zero. From t_{a3} to t_{a4} , current flows through v_s , L_{in} , Q_1 , C_{bus} , D_{R2} , D_4 , and Z_r , as shown in Fig. 9(c).

Stage 3 ($t_{a4} - t_{b1}$): At t_{a4} , Q_4 is turned ON. From t_{a4} to t_{b1} , Q_1 and Q_4 are ON, whereas Q_2 and Q_3 are OFF. At t_1 , input current i_{in} reaches zero. From t_{a4} to t_1 , current flows through v_s , L_{in} , Q_1 , C_{bus} , D_{R2} , Q_4 , and Z_r , as shown in Fig. 9(d). At t_2 , i_r changes polarity from negative to positive. From t_1 to t_{b1} , current flows through Q_1 , C_{bus} , Q_4 , and Z_r , as shown in Fig. 9(e) and (f).

Stage 4 ($t_{b1} - t_{b4}$): At t_{b1} , Q_4 is turned OFF; C_{s3} and C_{s4} start to be discharged and charged, respectively. From t_{b1} to t_{b3} , current flows through Q_1 , Z_r , C_{s3} , C_{s4} , and C_{bus} , as shown in Fig. 9(g). At t_{b3} , voltages of C_{s3} and C_{s4} reach zero and V_{bus} . From t_{b3} to t_{b4} , current flows through Q_1 , Z_r , and D_3 , as shown in Fig. 9(h).

Stage 5 ($t_{b4} - t_{c1}$): At t_{b4} , Q_3 is turned ON. From t_{b4} to t_{c1} , Q_1 and Q_3 are ON, whereas Q_2 and Q_4 are OFF. Current flows through Q_1 , Z_r , and Q_3 , as shown in Fig. 9(i).

Stage 6 ($t_{c1} - t_{c4}$): At t_{c1} , Q_1 is turned OFF; C_{s1} and C_{s2} start to be charged and discharged, respectively. From t_{c1} to t_{c3} , current flows through C_{s1} , C_{s2} , Z_r , Q_3 , and C_{bus} , as shown in Fig. 9(j). At t_{c2} , i_{in} starts to increase from zero. From t_{c2} to t_{c3} , current flows through v_s , L_{in} , C_{s1} , C_{s2} , Z_r , Q_3 , C_{bus} , and D_{R2} , as shown in Fig. 9(k). At t_{c3} , C_{s1} is charged to V_{bus} and C_{s2} is discharged to zero. From t_{c3} to t_{c4} , current flows through v_s , L_{in} , D_2 , Z_r , Q_3 , C_{bus} , and D_{R2} , as shown in Fig. 9(l).

Stage 7 ($t_{c4} - t_{d1}$): At t_{c4} , Q_2 is turned ON. From t_{c4} to t_{d1} , Q_2 and Q_3 are ON, whereas Q_1 and Q_4 are OFF. Current flows through v_s , L_{in} , Q_2 , Z_r , Q_3 , C_{bus} , and D_{R2} , as shown in Fig. 9(m) and (n). At t_3 , i_r changes polarity from positive to negative.

Stage 8 ($t_{d1} - t_{d4}$): At t_{d1} , Q_2 is turned OFF; C_{s1} starts to be discharged and C_{s2} starts to be charged. From t_{d1} to t_{d3} , current flows through v_s , L_{in} , C_{s1} , C_{s2} , C_{bus} , Q_3 , Z_r , and D_{R2} , as shown in Fig. 9(o). At t_{d3} , C_{s1} is discharged to zero and C_{s2} is charged to V_{bus} . From t_{d3} to t_{d4} , current flows through v_s , L_{in} , D_1 , V_{bus} , D_{R2} , Q_3 , and Z_r , as shown in Fig. 9(p).

Stage 9 ($t_{d4} - t_{Ts}$): At t_{d4} , Q_1 is turned ON, and this stage is the same with stage 1, as shown in Fig. 9(q).

3) Operation Frequency Selection: In order to realize soft switching of all the four switches in the proposed converter with the proposed modulation method, operation frequency f_s should be selected properly. First, by analyzing the operation of the converter, $i_1 - i_4$ as defined and shown in Fig. 8 have to be positive at the instances of $Q_1 - Q_4$ turning-off, respectively, so as to achieve soft switching in all four switches. Therefore, phase difference of $v_{AB,1}$ and i_r (defined as φ) must satisfy the following:

$$\varphi > [(1 - D_{ab})/2] \pi. \quad (49)$$

From (13) to (15), φ only varies with equivalent load resistance R_e (if operation frequency f_s is confirmed)

$$\varphi = \angle \frac{v_{AB}}{i_r} =$$

$$\angle \left(j\omega_s L_p - \frac{j}{\omega_s C_1} + \frac{\omega_s^2 M^2}{j\omega_s L_s - j/(\omega_s C_2) + R_e} \right). \quad (50)$$

Fig. 10(a) shows the curves of phase difference versus load resistance at different operation frequencies (curve 1: $\omega_s < \omega_1$; curve 2: $\omega_s = \omega_1$; curve 3: $\omega_1 < \omega_s < \omega_3$; curve 4: $\omega_s = \omega_3$; curve 5: $\omega_3 < \omega_s < \omega_2$; curve 6: $\omega_s = \omega_2$; curve 7: $\omega_s > \omega_2$). To obtain enough large φ , curves 6 and 7 should be selected. However, from (46) and (47), P_o will be infinitely large if ω_s is

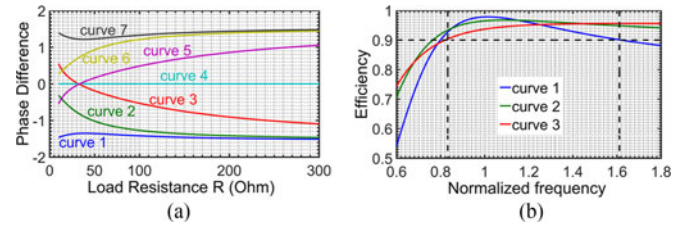


Fig. 10. (a) Phase difference versus R at different operation frequencies. (b) Efficiency versus normalized frequency at different load conditions.

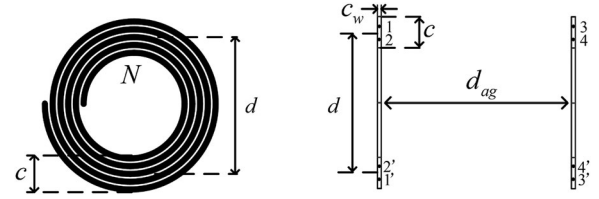


Fig. 11. Schematic of the resonant coils.

equal to ω_2 . Therefore, ω_s should be larger than ω_2 . Considering total equivalent series resistance (ESR) of the resonant tank, transmission efficiency characteristics of the resonant tank can be obtained at base frequency ω_3 , assuming ESR of primary and secondary sides to be 0.3Ω , as shown in Fig. 10(b) (curve 1: $R = 40 \Omega$; curve 2: $R = 100 \Omega$; curve 3: $R = 200 \Omega$). To maintain high efficiency, ω_s is suggested to be smaller than $1.6\omega_3$.

III. DESIGN PROCEDURE AND CONSIDERATIONS

A. Design Procedure

To facilitate production design of the proposed converter, a 2.56-kW laboratory prototype was designed to verify the proposed idea. The design procedures are described as follows.

1) Requirements of Input and Output: The input line voltage v_s is designed to be $220 V_{rms}$, 50 Hz. Maximum output power $P_{o,max}$ is 2.56 kW, with constant output voltage $V_o = 320 V$. Thus, maximum output current $I_{o,max}$ is 8 A.

2) Requirements and Design of Resonant Coils: First, the parameters of resonant coils need to be fixed. To simplify the design and calculations, the two coils (air core) are designed to be identical in spiral shape with the same wire type, mean coil diameter d , winding thickness c , and coils number N , as shown in Fig. 11. The operation frequency is set around 110 kHz in order to comply with the industrial wireless charging standard (SAE J1773). Skin effect is considered and then skin depth d_{sk} is obtained as

$$d_{sk} = \sqrt{(\rho/(\pi f_s \mu))} \approx 0.2 \text{ mm} \quad (51)$$

where ρ and μ are resistivity and permeability of copper. Therefore, copper litz wire is used to reduce the skin effect. The diameter of each thin wire strand should be smaller than twice of d_{sk} , 0.4 mm. Hence, the litz wire with the following parameters was chosen: diameter of each strand d_{st} is 0.2 mm; number of strands is 100; effective cross section area of the wire s_w is 3.14 mm^2 ; diameter of the wire c_w is 3.0 mm.

From [40], self-inductances of primary and secondary coils can be expressed as

$$L_p = L_s = \frac{0.3937((d/2) \times 100)^2 \cdot N^2 \cdot 10^{-6}}{8((d/2) \times 100) + 11(c \times 100)} = k_L N^2. \quad (52)$$

In practical implementation, c is determined by c_w , N , and air gap of loops c_{ag} (usually c_{ag} is 1.0 mm)

$$c = N(c_w + c_{ag}). \quad (53)$$

For mutual inductance calculation, primary coil is represented by two equivalent filaments 1, 1' and 2, 2', and secondary coil by 3, 3' and 4, 4', as shown in Fig. 11. Mutual inductance of the two coils can be calculated by

$$M = N^2 M_0 \quad (54)$$

$$M_0 = (M_{13} + M_{14} + M_{23} + M_{24})/4 \quad (55)$$

$$M_{ij} = f_k(r_i, r_j, d_{ag}) \cdot \sqrt{r_i \cdot r_j} \times 10^{-4} \quad (56)$$

where f_k is the function of k'^2 , obtained from tables in [41] and

$$k'^2 = \left[(r_i - r_j)^2 + d_{ag}^2 \right] / \left[(r_i + r_j)^2 + d_{ag}^2 \right] \quad (57)$$

where d_{ag} is air gap distance of two coils and

$$r_1 = r_3 = (d/2) \left[1 + c_w^2 / (6d^2) \right] + \sqrt{(c^2 - c_w^2) / 12} \quad (58)$$

$$r_2 = r_4 = (d/2) \left[1 + c_w^2 / (6d^2) \right] - \sqrt{(c^2 - c_w^2) / 12}. \quad (59)$$

For the application of wireless EV charging with typical automobile chassis size and height, d and d_{ag} are designed to be 500 and 200 mm, respectively. Considering in a loosely coupled WPT system, the coupling coefficient of two coils is around 0.1–0.3 [11], [42], the coupling coefficient k_{ps} is assumed to be 0.18, which also satisfies

$$k_{ps} = M / \sqrt{L_p L_s} = M_0 / k_L. \quad (60)$$

With the above known parameters and from (52) to (60), N is calculated to be 16. L_p and L_s are calculated to be 249.2 μ H and M is 44.8 μ H. In practical implementation, the measured values of L_p , L_s , and M are 241, 241, and 46 μ H, respectively.

Because of high core loss and low power density of coils with magnetic cores operating at high frequency (> 100 kHz), the resonant coils are designed without magnetic cores [9], [11]. In practical applications, shielding should be designed for WPT system; however, in the laboratory environment without strict EMI requirements, shielding is not designed for the prototype. There are existing research works on shielding design for WPT system [43]–[45], among which [44] using resonant reactive shielding coil is suitable for air-core coils.

3) Resonant Capacitors and Operation Frequency: The operation frequency f_s is chosen to be around 110 kHz. Make the higher resonant frequency [11] f_2 equal to 110 kHz and resonant capacitors are obtained by (19), which are measured

TABLE I
OPERATION POINTS AT DIFFERENT LOAD CONDITIONS

Load condition	P_o (W)	V_{bus} (V)	D_{ab}
100%	2560	637	1
80%	2048	600	0.88
60%	1536	592	0.75
40%	1024	622	0.63
20%	512	745	0.47

to be 11.83 nF in practical implementation. Then, the accurate higher resonant frequency is revised to be 104.8 kHz. Applying the proposed modulation method, D_{ab} is used to regulate the output voltage as load varies to maintain constant output voltage. When D_{ab} is equal to 1, output power should reach maximum 2.56 kW. In such condition, with the known parameters (L_p , L_s , M , C_1 , C_2 , V_{sp} , and V_o), assuming f_s to be 106 kHz (a little higher than 104.8 kHz), from (46) to (48), m is calculated to be 0.87, which cannot satisfy (5). Therefore, f_s needs to be revised. By calculation, f_s is chosen to be 111.6 kHz, at which m is equal to 0.49 satisfying (5).

4) Input Inductance L_{in} : From above, when in maximum output condition, operation parameters are obtained: $D_{ab} = 1$; $P_{in} = 2.56$ kW; $f_s = 111.6$ kHz; $m = 0.49$. Therefore, from (48), L_{in} is calculated to be 36.9 μ H. In practical implementation, L_{in} is measured to be 37.0 μ H. Here, L_{in} is designed to be air-core inductor because of high core loss and low power density if using a magnetic-core inductor. In the experimental prototype, appropriate measures are implemented to avoid the EMI problem due to the air-core inductor.

5) Load Range and Maximum Bus Voltage: Ideally P_{in} is equal to P_o and then (44) and (46)–(48) form a nonlinear equation set with three unknown parameters m , D_{ab} , and θ_k . By solving the equation set, V_{bus} and D_{ab} at different load conditions are calculated, as shown in Table I. By calculations and analysis, at low load conditions, m value decreases with load power decreasing. Therefore, the minimum output power is limited by minimum m value (maximum V_{bus}). Here, the minimum output power is set as 20% of rated output power, which is 512 W, and the corresponding m value is 0.417. Therefore, maximum bus voltage is 745 V.

6) Design of Input EMI Filter: To design the input EMI filter of the proposed converter, the input impedance of the proposed converter needs to be obtained. Because input part of the proposed converter acts as a DCM boost PFC converter, input impedance characteristics can be analyzed like that of a DCM boost PFC converter. From [46], input impedance of the proposed converter Z_{ic} is given as

$$Z_{ic} = \frac{8L_{in}f_s(V_{bus} - v_s)}{D_{ab}^2 V_{bus}} \frac{1 + s / \left(\frac{D_{ab}^2}{8L_{in}C_{bus}f_s} \frac{v_s^2(2V_{bus} - v_s)}{V_{bus}(V_{bus} - v_s)^2} \right)}{1 + s / \left(\frac{D_{ab}^2}{8L_{in}C_{bus}f_s} \frac{v_s^2(2V_{bus} - v_s)}{V_{bus}^2(V_{bus} - v_s)} \right)}. \quad (61)$$

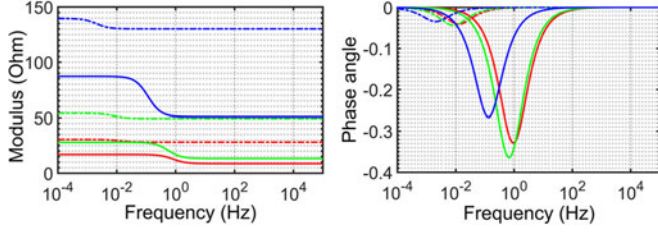


Fig. 12. Input impedance characteristics of the proposed converter at different load condition: red curves: 100% load; green curves: 60% load; blue curves: 20% load and solid lines are those with instant line voltage 311 V; dotted lines are those with instant line voltage 50 V.

From Fig. 12, at line frequency 50 Hz, input impedance of the proposed converter is almost resistive at all load conditions, which can be noted as the input resistance R_{in} . Minimum R_{in} occurs in 100% load condition with v_s to be V_{sp} (311 V) and maximum R_{in} occurs in 20% load condition with v_s to be zero

$$R_{in.min} \approx (8L_{in}f_s / D_{ab.100\%})^2 (1 - V_{sp} / V_{bus.100\%})^2 = 8.7 \Omega$$

$$R_{in.max} \approx 8L_{in}f_s / D_{ab.20\%}^2 = 149.5 \Omega. \quad (62)$$

An LC low-pass filter is implemented with inductor and capacitor noted as L_{if} and C_{if} . Assuming voltage out from input EMI filter is ideally the same as input voltage, in order to avoid phase shift of input current, impedance of C_{if} at 50 Hz is required to be much larger than $R_{in.max}$

$$1/(\omega_l C_{if}) \gg R_{in.max} \Rightarrow C_{if} \ll 21.3 \mu F. \quad (63)$$

Therefore, C_{if} is designed to be $1.0 \mu F$. And, in order to make voltage out from input EMI filter close to input voltage as much as possible, impedance of L_{if} at 50 Hz is required to be much smaller than $R_{in.min}$

$$\omega_l L_{if} \ll R_{in.min} \Rightarrow L_{if} \ll 27.5 \text{ mH}. \quad (64)$$

Hence, L_{if} is designed to be 1.0 mH with measured ESR R_{lf} to be 0.1Ω . With the parameters, output impedance of the input EMI filter is

$$Z_{of} = \frac{(1/(sC_{if}))(sL_{if} + R_{lf})}{1/(sC_{if}) + sL_{if} + R_{lf}} = \frac{sL_{if} + R_{lf}}{s^2 L_{if} C_{if} + sR_{lf} C_{if} + 1}. \quad (65)$$

And therefore, transfer function of the input EMI filter is

$$F_f = Z_{ic} / [Z_{ic} + Z_{of}] = 1 / [1 + Z_{of} / Z_{ic}]. \quad (66)$$

By calculation and analysis, Z_{of}/Z_{ic} , regarded as the open-loop gain, fulfilled the Nyquist stability criterion at different load conditions. Hence, there is no possible instability problem due to interaction with the input EMI filter.

Because current flowing through L_{if} is 50 Hz, core loss is very small and can be ignored compared to copper loss. Hence, the loss of the input EMI filter can be calculated by

$$P_{f.loss} = i_{in.rms}^2 \cdot R_{lf} \quad (67)$$

where $i_{in.rms}$ can be calculated with (9). Therefore, at 100% load condition, loss of input EMI filter is calculated to be 13.6 W, about 0.5% of the load power, which is acceptable.

TABLE II
PARAMETERS OF THE LABORATORY PROTOTYPE

Components	Details
L_{in}	37.0 μH (air-core inductor)
D_{R1}, D_{R2}	IXYS DSEI 2x31-10B
Q_1, Q_2, Q_3, Q_4	CREE CAS120M12BM2
C_{bus}	4950 μF , 900 V (electrolytic capacitors bank)
C_{s1}, C_{s2}	5 nF, 1 kV (polypropylene capacitors)
C_{s3}, C_{s4}	1 nF, 1 kV (polypropylene capacitors)
L_p, L_s, M	241 μH ; 241 μH ; 46 μH
C_1, C_2	11.83 nF; 11.83 nF (5-kV polypropylene capacitors)
$D_{s1}, D_{s2}, D_{s3}, D_{s4}$	Vishay VS-30EPH06PbF
C_f	220 μF , 450 V (electrolytic capacitor)
L_{if}, C_{if}	1.0 mH, 1.0 μF

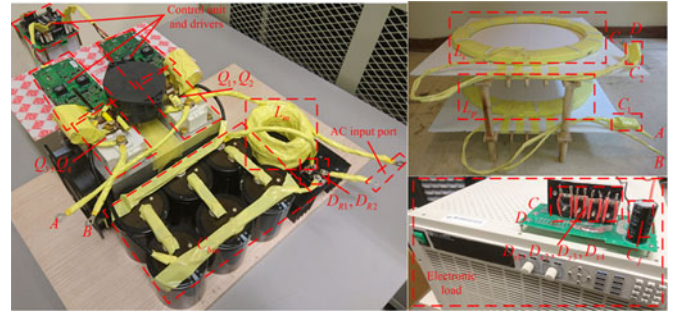


Fig. 13. Setup of the laboratory prototype.

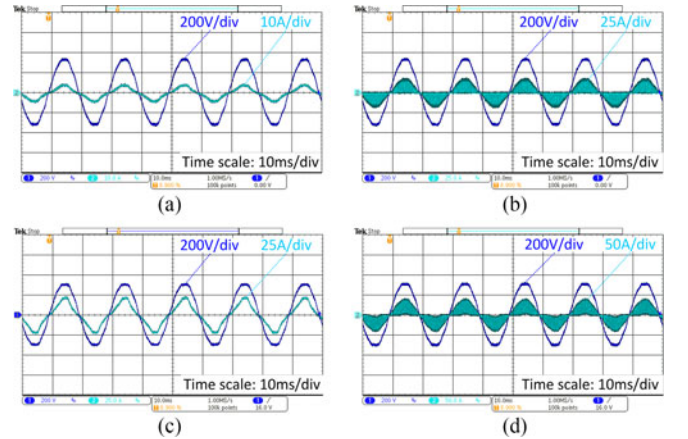


Fig. 14. Input voltage (in dark blue) and current (in light blue): (a) with EMI filter, 20% load; (b) without EMI filter, 20% load; (c) with EMI filter, 100% load; and (d) without EMI filter, 100% load.

B. Design Summary and Laboratory Prototype

Table II shows the design summary and component selection of the laboratory prototype. For $Q_1 - Q_4$, two SiC half-bridge MOSFET modules with 1.2-kV voltage rating are used. Fig. 13 shows the setup of the laboratory prototype.

IV. EXPERIMENTAL RESULTS

Referring to the proposed design procedure, the laboratory prototype with rated (100% load) 2.56-kW output is built and tested at different load conditions. Fig. 14 shows the waveforms of ac line input voltage and current and Fig. 15(b) shows the

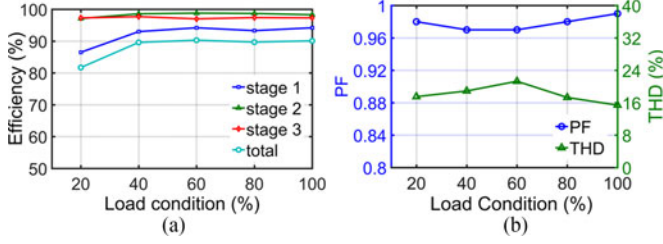


Fig. 15. (a) Efficiencies under different load conditions at different stages. (b) PF and THD_i under different load conditions.

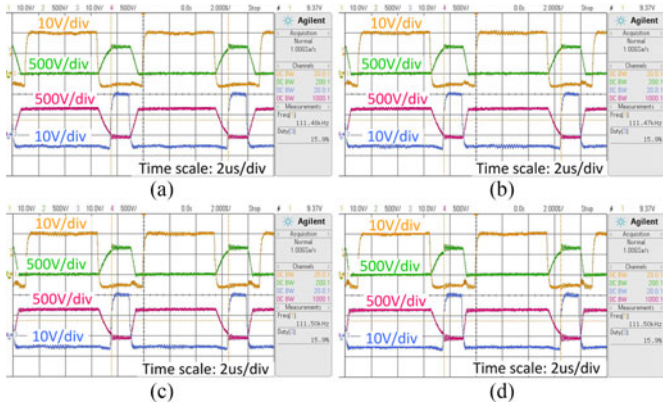


Fig. 16. Switching waveforms of Q_1 and Q_2 with 20% load under different phase of input line voltage: (a) 0; (b) $\pi/6$; (c) $\pi/3$; and (d) $\pi/2$ (v_{g1} and v_{Q1} in yellow and green; v_{g2} and v_{Q2} in blue and violet).

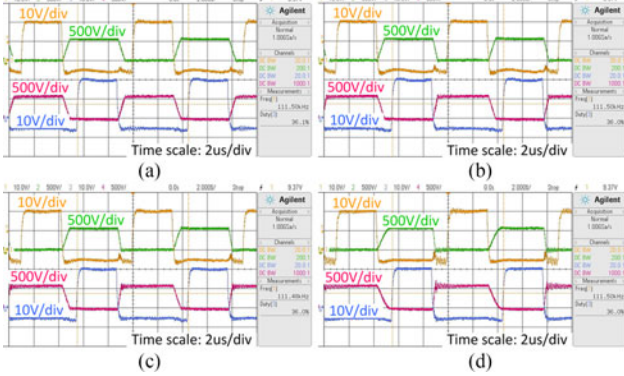


Fig. 17. Soft switching waveforms of Q_1 and Q_2 with 100% load under different phase of input line voltage: (a) 0; (b) $\pi/6$; (c) $\pi/3$; and (d) $\pi/2$ (v_{g1} and v_{Q1} in yellow and green; v_{g2} and v_{Q2} in blue and violet).

PF of ac line input and THD of ac line current (THD_i). At rated load condition, the PF and THD_i reach 0.99 and 15.4%, respectively. Overall, from 20% to 100% load range, the PF is over 0.97 and THD_i is below 22%. The ac line input voltage is not completely a pure sinewave (with measured THD 3%). If ac line input voltage's THD is close to zero, then THD_i can be 3%–4% further lower than present measured values. Fig. 15(a) shows the total efficiency and partial efficiencies at different stages (stage 1: from ac line input to input port (AB) of resonant tank; stage 2: from input port (AB) to output port (CD) of resonant tank; stage 3: from output port (CD) of resonant tank to load). At rated load condition, total efficiency reaches 90.1% and efficiency of resonant tank (stage 2) reaches 98.3%. From

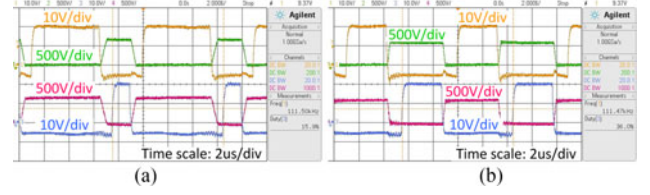


Fig. 18. Soft switching waveforms of Q_3 and Q_4 : (a) 20% load; and (b) 100% load (v_{g3} and v_{Q3} in yellow and green; v_{g4} and v_{Q4} in blue and violet).

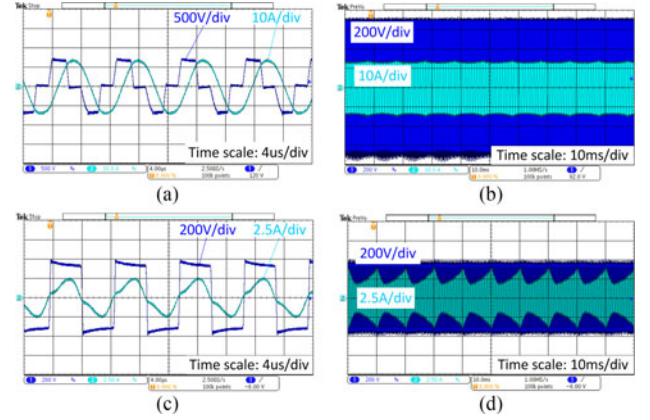


Fig. 19. Voltage (in dark blue) and current (in light blue) of resonant tank under 20% load condition: (a) primary side, high frequency profile; (b) primary side, low frequency (50 Hz) profile; (c) secondary side, high frequency profile; and (d) secondary side, low frequency (50 Hz) profile.

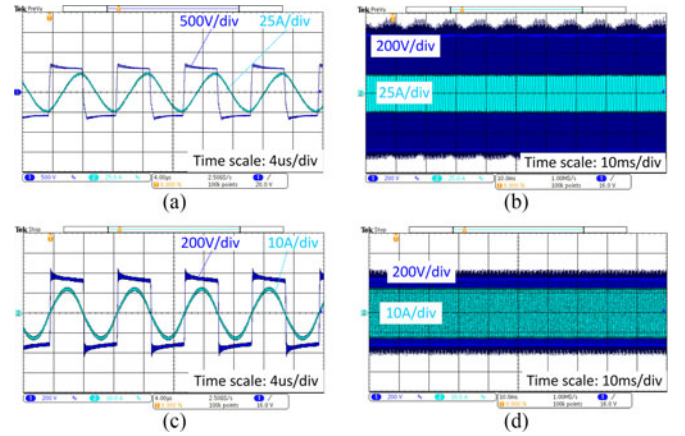


Fig. 20. Voltage (in dark blue) and current (in light blue) of resonant tank under 100% load condition: (a) primary side, high frequency profile; (b) primary side, low frequency (50 Hz) profile; (c) secondary side, high frequency profile; and (d) secondary side, low frequency (50 Hz) profile.

40% to 100% load range, total efficiency maintains as high as 90%. However, at 20% load condition, total efficiency drops to 81.7% because switching loss of Q_1 and Q_2 increases as soft switching cannot be realized completely due to insufficient resonant current. Fig. 16 shows the switching waveforms of Q_1 and Q_2 at 20% load condition. Fig. 17 shows the soft-switching waveforms of Q_1 and Q_2 at 100% load condition. Fig. 18 shows the soft-switching waveforms of Q_3 and Q_4 at both 20% and 100% load conditions. Figs. 19 and 20 show the voltage and current waveforms of resonant tank at 20% and

TABLE III
COMPARISON OF WPT SYSTEM TOPOLOGIES

Topologies	Efficiency (%)	Power factor	THD _i (%)	Number of semiconductor devices
Proposed single-stage WPT converter	90.1	0.99	15.4	6 diodes + 4 switches
Traditional two-stage converter for WPT	86.8	0.99	15.7	9 diodes + 5 switches
Traditional converter without PFC for WPT	92.2	0.69	96.5	8 diodes + 4 switches
Z-source converter with PFC for WPT	72.1	0.987	15.67	8 diodes + 4 switches

100% load condition, respectively. For comparison, a traditional two-stage topology for WPT with separate boost DCM PFC and a traditional topology for WPT without PFC are built up and tested. Table III shows the comparison results at 100% load condition in terms of efficiency, PF, THD_i, and number of semiconductor devices. The Z-source resonant converter with PFC for WPT proposed in [36] is also compared in Table III. Generally, the proposed topology exhibits its advantages compared to the other three topologies.

V. CONCLUSION AND FUTURE WORK

In this paper, a single-stage topology with bridgeless boost PFC rectifier was proposed to apply in a high-power WPT system for the first time. Compared to the traditional WPT system with a separate boost PFC converter, the proposed topology was observed to be more efficient and economical because of the less number of semiconductor components. Detailed analysis of the proposed topology, design procedure, and example were presented. Finally, a 2.56-kW experimental prototype was implemented and tested to prove its high efficiency, PFC functionality, and economy. Future research will focus on improving its efficiency and reducing bus voltage of the proposed topology at light load conditions as well as issues in EMI and shielding.

REFERENCES

- [1] Y. Jang and M. M. Jovanovic, "A contactless electrical energy transmission system for portable-telephone battery chargers," *IEEE Trans. Ind. Electron.*, vol. 50, no. 3, pp. 520–527, Mar. 2003.
- [2] G. B. Joung and B. H. Cho, "An energy transmission system for an artificial heart using leakage inductance compensation of transcutaneous transformer," *IEEE Trans. Power Electron.*, vol. 13, no. 6, pp. 1013–1022, Nov. 1998.
- [3] Y. Wang and D. Ma, "Design of integrated dual-loop Δ - Σ modulated switching power converter for adaptive wireless powering in biomedical implants," *IEEE Trans. Ind. Electron.*, vol. 58, no. 9, pp. 4241–4249, Sep. 2011.
- [4] D. Ahn and S. Hong, "Wireless power transmission with self-regulated output voltage for biomedical implant," *IEEE Trans. Ind. Electron.*, vol. 61, no. 5, pp. 2225–2235, May 2014.
- [5] S. Li and C. C. Mi, "Wireless power transfer for electric vehicle applications," *IEEE J. Emerg. Sel. Topics Power Electron.*, vol. 3, no. 1, pp. 4–17, Mar. 2015.
- [6] C. S. Wang, O. H. Stielau, and G. A. Covic, "Design considerations for a contactless electric vehicle battery charger," *IEEE Trans. Ind. Electron.*, vol. 52, no. 5, pp. 1308–1313, Oct. 2005.
- [7] J. Shin *et al.*, "Design and implementation of shaped magnetic resonance based wireless power transfer system for roadway-powered moving electric vehicles," *IEEE Trans. Ind. Electron.*, vol. 61, no. 3, pp. 1179–1192, Mar. 2014.
- [8] G. A. Covic, J. T. Boys, M. L. G. Kissin, and H. G. Lu, "A three-phase inductive power transfer system for roadway-powered vehicles," *IEEE Trans. Ind. Electron.*, vol. 54, no. 6, pp. 3370–3378, Dec. 2007.
- [9] N. L. Zhen, R. A. Chinga, R. Tseng, and L. Jenschan, "Design and test of a high-power high-efficiency loosely coupled planar wireless power transfer system," *IEEE Trans. Ind. Electron.*, vol. 56, no. 5, pp. 1801–1812, May 2009.
- [10] J. J. Casanova, Z. N. Low, and J. Lin, "A loosely coupled planar wireless power system for multiple receivers," *IEEE Trans. Ind. Electron.*, vol. 56, no. 8, pp. 3060–3068, Aug. 2009.
- [11] S. C. Moon, B. C. Kim, S. Y. Cho, C. H. Ahn, and G. W. Moon, "Analysis and design of a wireless power transfer system with an intermediate coil for high efficiency," *IEEE Trans. Ind. Electron.*, vol. 61, no. 11, pp. 5861–5870, Nov. 2014.
- [12] D. Ahn and S. Hong, "A study on magnetic field repeater in wireless power transfer," *IEEE Trans. Ind. Electron.*, vol. 60, no. 1, pp. 360–371, Jan. 2013.
- [13] U. K. Madawala and D. J. Thrimawithana, "A bidirectional inductive power interface for electric vehicles in V2G systems," *IEEE Trans. Ind. Electron.*, vol. 58, no. 10, pp. 4789–4896, Oct. 2011.
- [14] A. J. Moradewicz and M. P. Kazmierkowski, "Contactless energy transfer system with FPGA-controlled resonant converter," *IEEE Trans. Ind. Electron.*, vol. 57, no. 9, pp. 3181–3190, Sep. 2010.
- [15] B. L. Cannon, J. F. Hoburg, D. D. Stancil, and S. C. Goldstein, "Magnetic resonant coupling as a potential means for wireless power transfer to multiple small receivers," *IEEE Trans. Power Electron.*, vol. 24, no. 7, pp. 1819–1825, Jul. 2009.
- [16] T. C. Beh, M. Kato, T. Imura, S. Oh, and Y. Hori, "Automated impedance matching system for robust wireless power transfer via magnetic resonance coupling," *IEEE Trans. Ind. Electron.*, vol. 60, no. 9, pp. 3689–3698, Sep. 2013.
- [17] C. Linhui, L. Shuo, C. Z. Yong, and J. C. Tie, "An optimizable circuit structure for high-efficiency wireless power transfer," *IEEE Trans. Ind. Electron.*, vol. 60, no. 1, pp. 339–349, Jan. 2013.
- [18] R. Johari, J. V. Krogmeire, and D. J. Love, "Analysis and practical considerations in implementing multiple transmitters for wireless power transfer via coupled magnetic resonance," *IEEE Trans. Ind. Electron.*, vol. 61, no. 4, pp. 1774–1783, Apr. 2013.
- [19] A. P. Sample, D. A. Meyer, and J. R. Smith, "Analysis, experimental results, and range adaptation of magnetically coupled resonators for wireless power transfer," *IEEE Trans. Ind. Electron.*, vol. 58, no. 2, pp. 544–554, Feb. 2011.
- [20] T. Imura and Y. Hori, "Maximizing air gap and efficiency of magnetic resonant coupling for wireless power transfer using equivalent circuit and Neumann formula," *IEEE Trans. Ind. Electron.*, vol. 58, no. 10, pp. 4746–4752, Oct. 2011.
- [21] A. Kurs, A. Karalis, R. Moffatt, J. D. Joannopoulos, P. Fisher, and M. Soljačić, "Wireless power transfer via strongly coupled magnetic resonances," *Sci. Express*, vol. 317, no. 5834, pp. 83–86, Jun. 7, 2007.
- [22] G. Moschopoulos and P. Jain, "Single phase single stage power factor corrected-converter topologies," *IEEE Trans. Ind. Electron.*, vol. 52, no. 1, pp. 23–35, Feb. 2005.
- [23] B. Singh, B. N. Singh, A. Chandra, K. Al-Haddad, A. Pandey, and D. P. Kothari, "A review of single-phase improved power quality AC-DC converters," *IEEE Trans. Ind. Electron.*, vol. 50, no. 5, pp. 962–981, Oct. 2003.
- [24] M. Qiu, G. Moschopoulos, H. Pinheiro, and P. Jain, "Analysis and design of a single stage power factor corrected full-bridge converter," in *Proc. IEEE Appl. Power Electron. Conf. Expo.*, 1999, pp. 119–125.
- [25] F. S. Kang, S. J. Park, and C. U. Kim, "ZVZCS single-stage PFC AC-to-DC half-bridge converter," *IEEE Trans. Ind. Electron.*, vol. 49, no. 1, pp. 206–216, Feb. 2002.
- [26] S. Chen, Z. Li, and C. Chen, "Analysis and design of single-stage AC/DC LLC resonant converter," *IEEE Trans. Ind. Electron.*, vol. 59, no. 3, pp. 1538–1544, Mar. 2012.
- [27] C. M. Lai, R. C. Lee, T. W. Wang, and K. K. Shyu, "Design and implementation of a single-stage LLC resonant converter with high power factor," in *Proc. IEEE Int. Symp. Ind. Electron.*, Jun. 2007, pp. 455–460.

- [28] C. Lai and R. Lee, "A single-stage AC/DC LLC resonant converter," in *Proc. Int. Conf. Ind. Technol.*, 2006, pp. 1386–1390.
- [29] D. D. C. Lu, H. H. C. Lu, and V. Pjevalica, "Single-stage AC/DC boost-forward converter with high power factor and regulated bus and output voltages," *IEEE Trans. Ind. Electron.*, vol. 56, no. 6, pp. 2128–2132, Jun. 2009.
- [30] J. J. Lee, J. M. Kwon, E. H. Kim, W. Y. Choi, and B. H. Kwon, "Single-stage single-switch PFC flyback converter using a synchronous rectifier," *IEEE Trans. Ind. Electron.*, vol. 55, no. 3, pp. 1352–1365, Mar. 2008.
- [31] S. C. Moon, G. B. Koo, and G. W. Moon, "A new control method of interleaved single-stage flyback AC–DC converter for outdoor LED lighting systems," *IEEE Trans. Power Electron.*, vol. 28, no. 8, pp. 4051–4062, Aug. 2013.
- [32] R. Martinez and P. N. Enjeti, "A high-performance single-phase rectifier with input power factor correction," *IEEE Trans. Power Electron.*, vol. 11, no. 2, pp. 311–317, Mar. 1996.
- [33] J. W. Lim and B. H. Kwon, "A power factor controller for single-phase PWM rectifiers," *IEEE Trans. Ind. Electron.*, vol. 46, no. 5, pp. 1035–1037, Oct. 1999.
- [34] J. Salmon, "Circuit topologies for PWM boost rectifiers operated from 1-phase and 3-phase AC supplies and using either single or split DC rail voltage outputs," in *Proc. Appl. Power Electron. Conf. Expo.*, 1995, vol. 1, pp. 473–479.
- [35] L. Huber, J. Yungtaek, and M. M. Jovanovic, "Performance evaluation of bridgeless PFC boost rectifier," *IEEE Trans. Power Electron.*, vol. 23, no. 3, pp. 1381–1390, May 2008.
- [36] N. S. González-Santini, H. Zeng, Y. Yu, and F. Z. Peng, "Z-source resonant converter with power factor correction for wireless power transfer applications," *IEEE Trans. Power Electron.*, vol. 31, no. 11, pp. 7691–7700, Nov. 2016.
- [37] W. Y. Choi and J. S. Yoo, "A bridgeless single-stage half-bridge AC/DC converter," *IEEE Trans. Power Electron.*, vol. 26, no. 12, pp. 3884–3895, Dec. 2011.
- [38] STMicroelectronics Group of Companies, "LLC resonant half-bridge converter design guideline," STMicroelectronics, Geneva, Switzerland, Appl. Note AN2450, Mar. 2014.
- [39] W. Zhang, S. C. Wong, C. K. Tse, and Q. Chen, "Design for efficiency optimization and voltage controllability of series-series compensated inductive power transfer systems," *IEEE Trans. Power Electron.*, vol. 29, no. 1, pp. 191–200, Jan. 2014.
- [40] Microchip Technology Inc., "Antenna circuit design for RFID applications," Microchip Technology Inc., Chandler, AZ, USA, Appl. Note AN710, 2003.
- [41] F. W. Grover, "Mutual inductance of coaxial circular filaments," in *Inductance Calculations: Working Formulas and Tables*, 1st ed. Mineola, NY, USA: Dover, 2004, ch. 11, sec. ii, pp. 77–87.
- [42] W. X. Zhong and S. Y. R. Hui, "Maximum energy efficiency tracking for wireless power transfer systems," *IEEE Trans. Power Electron.*, vol. 30, no. 7, pp. 4025–4034, Jul. 2015.
- [43] X. Liu and S. Y. R. Hui, "An analysis of a double-layer electromagnetic shield for a universal contactless battery charging platform," in *Proc. 36th IEEE Power Electron. Spec. Conf.*, Jun. 2005, pp. 1767–1772.
- [44] J. Park *et al.*, "A resonant reactive shielding for planar wireless power transfer system in smartphone application," *IEEE Trans. Electromagn. Compat.*, vol. 59, no. 2, pp. 695–703, Apr. 2017.
- [45] B. K. Kushwaha, G. Rituraj, and P. Kumar, "3-D analytical model for computation of mutual inductance for different misalignments with shielding in wireless power transfer system," *IEEE Trans. Transport. Electrific.*, vol. 3, no. 2, pp. 332–342, Jun. 2017.
- [46] V. Grigore, J. Kyyra, and J. Rajamaki, "Input filter design for power factor correction converters operating in discontinuous conduction mode," in *Proc. IEEE Electromagn. Compat.*, 1999, pp. 145–150.



Junwei Liu received the B.Eng. degree in water conservancy and hydropower engineering from Huazhong University of Science and Technology, Wuhan, China, in 2012. He is currently working toward the Ph.D. degree in electrical engineering at the Department of Electrical Engineering, The Hong Kong Polytechnic University, Hong Kong.

His research interests include wireless power transfer, ac–dc single-stage topologies, and high-power dc–dc conversions.



Ka Wing Chan (M'98) received the B.Sc. (Hons.) and Ph.D. degrees in electronic and electrical engineering from the University of Bath, Bath, U.K., in 1988 and 1992, respectively.

He is currently an Associate Professor and Associate Head in the Department of Electrical Engineering, The Hong Kong Polytechnic University, Hong Kong. His research interests include power system stability, analysis and control, power grid integration, security, resilience and optimization, demand response management, etc.



Chi Yung Chung (M'01–SM'07–F'16) received the B.Eng. (with First Class Hons.) and Ph.D. degrees in electrical engineering from The Hong Kong Polytechnic University, Hong Kong, in 1995 and 1999, respectively.

He was with the Powertech Labs, Inc., Surrey, BC, Canada, the University of Alberta, Edmonton, AB, Canada, and The Hong Kong Polytechnic University. He is currently a Professor and the SaskPower Chair of power systems engineering in the Department of Electrical and Computer Engineering, University of Saskatchewan, Saskatoon, SK, Canada. His research interests include power system stability/control, planning and operation, computational intelligence applications, power markets, and electric vehicle charging.

Prof. Chung is an Editor of the *IEEE TRANSACTIONS ON SUSTAINABLE ENERGY* and an Associate Editor of *IET Generation, Transmission, and Distribution*. He is also a Member-at-Large (Smart Grid) of the IEEE PES Governing Board.



Nelson Hon Lung Chan received the B.Eng. and Ph.D. degrees in electrical engineering from the Department of Electrical Engineering, The Hong Kong Polytechnic University (HKPolyU), Hong Kong, in 1996 and 2000, respectively.

Since 2010, he has been a Senior Research Fellow at HKPolyU. His research interests include power electronics, power system, control theory, and artificial intelligence.



Ming Liu received the B.Eng. degree in electrical engineering from Qingdao University, Qingdao, China, in 2014. He is currently working toward the Ph.D. degree in electrical engineering at the Department of Electrical Engineering, The Hong Kong Polytechnic University, Hong Kong.

His research interests include electric machine design and control, wireless power transfer topologies, and finite element analysis.



Wenzheng Xu received the B.Eng. degree from the Department of Electrical Engineering, Beijing Jiaotong University, Beijing, China, in 2012, and the M.Sc. degree from the Department of Electrical and Electronic Engineering, The University of Hong Kong, Hong Kong, in 2013. He is currently working toward the Ph.D. degree in the Department of Electrical Engineering, The Hong Kong Polytechnic University, Hong Kong, all in electrical engineering.

His research interests include power electronics topologies and control of bidirectional converters.